Applied Catalysis B: Environmental 192 (2016) 26–34

Contents lists available at ScienceDirect

Applied Catalysis B: Environmental

journal homepage: www.elsevier.com/locate/apcatb

A solution-based procedure for synthesis of nitrogen doped graphene as an efficient electrocatalyst for oxygen reduction reactions in acidic and alkaline electrolytes

Edip Bayram [a,*], Gizem Yilmaz [b], Sanjeev Mukerjee [b]

[a] Akdeniz University Department of Chemistry, 07058 Antalya, Turkey
[b] Department of Chemistry and Chemical Biology, Center of Renewable Energy Technology (NUCRET), Northeastern University, 360 Huntington Avenue, Boston, MA 02115, USA

ARTICLE INFO

Article history:
Received 9 January 2016
Received in revised form 15 March 2016
Accepted 21 March 2016
Available online 23 March 2016

Keywords:
Nitrogen doped graphene
Electrocatalyst
Oxygen reduction reaction (ORR)
Methanol-tolerant
Fuel cell

ABSTRACT

A nitrogen-doped graphene (N-GN) based electrocatalysts have been synthesized by a two-step solution-based scalable procedure of direct annealing of grapheneoxide (GO)/melamine gel mixture. The specific surface area (SSA) of GO has been increased through the pre-gelation of melamine on GO sheets as spacing. Despite the low nitrogen content, the N-GNs displayed much more oxygen reduction reaction (ORR) activities with positive onset potentials and large current densities than the blank sample. Moreover, compared with the high quality commercial (46%) Pt/C, N-GN15 exhibits higher current density and excellent tolerance to methanol crossover effect in both acidic and alkaline electrolytes making it an economic noble metal-free candidate for practical fuel cells. The higher current densities of N-GNs over blank sample and Pt/C have been linked to the synergetic effect of surface graphitic N groups and larger SSA of N-GNs.

1. Introduction

Displacement of precious metal electrocatalysts with commercially available and inexpensive materials which facilitates the sluggish cathodic oxygen reduction reaction (ORR) is a key issue in the development of fuel cells and air batteries. The traditional Pt-based catalyst exhibits high catalytic activity and is being continuously optimized in many ways, including tailoring the size-, shape- and alloy-effect [1–3]. However, the scarcity and high cost of Pt limit the large-scale production and commercialization of Pt-loaded fuel cells. According to the cost analysis, Pt-based catalysts account for almost 34% of fuel cell stack cost [4]. In addition, the Pt-based catalyst also suffers from crossover and poisoning effects, which limits the efficiency of fuel cells [5]. The search for alternative ORR catalysts has led to the development of many non-precious metal catalysts, such as transition metal-microcycles [6] nanostructured manganese oxides [7] and metal-free nitrogen doped carbon materials [8,9]. It was reported that the nitrogen doped carbon materials not only have high activity toward ORR, but also long-term durability and tolerance to methanol and CO poisoning [10].

Graphene is a flexible and expandable two-dimensional (2D) monolayer carbon material consisting of sp^2 carbon atoms [11,12]. Graphene itself is an excellent alternative as electrode material and great efforts have been made to utilize graphene based nanomaterials as promising electrode materials for ORR due to the unique chemistry of the edges of a graphene sheet, the mechanical strength, high thermal and chemical stability, high electrical conductivity, large surface area and abounding functional groups involved [12–16]. Since the chemically stable sp^2-hybridized carbon network in graphene hinders its application in chemistry, particularly in catalysis, various strategies have been employed to tailor the electronic properties and open up the band gap of graphene via physical and chemical means. Both theoretical calculations and experiments have proved that chemical doping with heteroatoms like N or B can modify the properties of carbon materials [17,18].

Several methods have been carried out for doping graphene sheets by N atoms. Generally, these methods can be categorized into two groups: in situ direct-doping and post-doping. In situ direct-doping route usually employs appropriate N/C containing molecules as precursors to rearrange nitrogen and carbon atoms over metal catalysts at high temperature [19]. Post-doping route involves the preparation of carbons and subsequent post treatment in nitrogen-containing atmospheres, such as NH_3, N-ion plasma

* Corresponding author.
E-mail address: ebayram@akdeniz.edu.tr (E. Bayram).

http://dx.doi.org/10.1016/j.apcatb.2016.03.043
0926-3373/

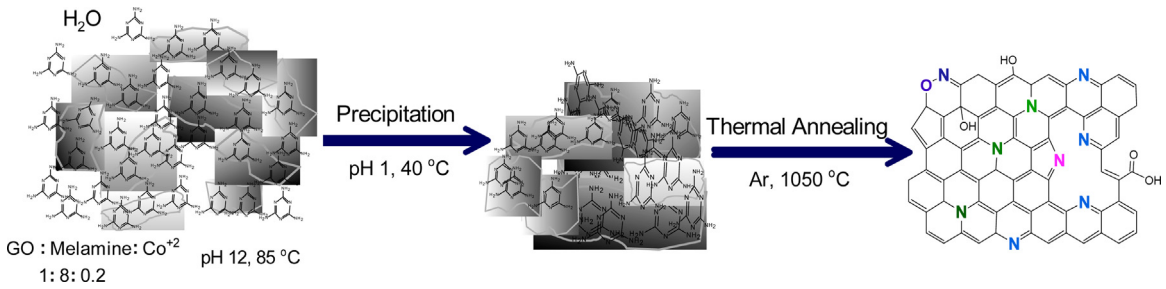

Fig. 1. Schematic representation of synthesis procedure for the N-GN catalysts.

[20]. The synthesis methods and ORR performances of N-doped graphene (N-GN) nanomaterials has recently been reviewed [21].

In addition to N doping, accurate control of the fine morphologies of the final products also plays a significant role in enhancing ORR activities of N-GN. Due to the nature of the 2D material, graphene nanosheets tend to stack together through π–π interaction during the application [21,22]. The stacking blocks a substantial amount of catalytic sites on graphene and unavoidably decreases the catalytic activity. In this regard, great contributions have been made to design high performance N-GN nanomaterials aiming to enlarge the specific surface area (SSA) and further improve their electrochemical activities. N-GN-based composite sheets were prepared by carbonizing a mixture of GO and phenol–melamine–formaldehyde pre-polymer in the presence of a soft template. The resultant composite exhibited high electrocatalytic activity, good durability and high selectivity for the ORR [23]. Qu and colleagues synthesized an N-GN framework through thermal treatment of grapheneoxide and pyrrole and subsequent freeze-drying and annealing. Owing to the synergetic function of the 3D open-pore structure and high N content, this 3D N-GN showed high electrocatalytic activity for ORR [24].

This study reports a low cost and scalable procedure for the synthesis of N-GN having high electrocatalytic activity for ORR by direct pyrolysis of GO/melamine gel. GO/melamine gel was prepared through a solution-based method. With the pyrolysis of dried GO/melamine gel in Ar atmosphere at 1050 °C, N atoms were doped into the suitable positions of the GO sheets, resulting in the formation of N-GN. Efficiently avoided reaggregation with the melamine as spacing, obtained N-GN showed increased SSA. In spite of the poor N content, N-GN samples exhibited much enhanced ORR electrocatalytic activity and strong methanol tolerant capability in both acidic and alkali media.

2. Experimental

2.1. Materials

Graphene oxide was from XG Sciences coded as xGnP-M-5. Melamine, HCl, KOH and $Co(NO_3)_2{\cdot}6H_2O$ were purchased from Sigma-Aldrich while 70% double distilled $HClO_4$ from GFS Chemicals. A 46% Pt/C catalyst from Tanaka was used for comparison. All chemicals were used as received without any further purification. High purity water used in all experiments was from 18.2 MΩ Milli-Q UV (Millipore) water system.

2.2. Catalyst preparation

Synthesis procedure for the N-GN catalysts has been depicted in Fig. 1. Briefly, certain amount of GO and melamine (w/w) were mixed in 30 mL deionized water and sonicated for 30 min. Then, pH of the dispersion was adjusted to pH 12 using 2 M NaOH solutions. The resultant mixture was heated to 85 °C, then catalytic amount of $Co(NO_3)_2{\cdot}6H_2O$ (molar ratio of melamine to Co^{+2} was 40:1) was added into the dispersion and maintained at this temperature for 30 min with continuous stirring until a viscous gel mixture was obtained. The mixture was cooled down to 40 °C and the pH value was adjusted to 2 using 6 M HCl. After this step, the viscous gel mixture turned into a solid. The resulting solid was cured at 85 °C for 72 h in a vacuum oven and bright solid was obtained (Fig. S1). Bright solid was grinded, washed with deionized water until neutral pH to remove the residual ions including Co^{+2}. Finally, the dried powder was annealed at 1050 °C for 1 h under a high purity Ar atmosphere with a gas flow rate of 30 mLmin^{-1} and heating rate of 10 °C min^{-1}. The prepared catalysts were labeled as N-GN15, N-GN10 and N-GN5. Digits represent GO weight percent in dry GO-melamine mixture. A blank sample was also prepared following the same route, but without adding melamine, and labeled as rGO.

2.3. Characterization of catalyst

The scanning electron microscopy (SEM) was performed on a Hitachi S-4900 FSEM field-emitting scanning electron microscope with an accelerating voltage of 5 kV. The nitrogen adsorption and desorption isotherms were measured at the temperature of liquid nitrogen (77 K) using a QUADRASORB SI automated surface area analyzer (Quantachrome Corporation, USA). Specific surface area was calculated from the adsorption branch according to the Brunauer–Emmett–Teller (BET) method. Powder XRD patterns were recorded by using an X ray diffractometer (Rigaku model Ultima-IV) using CuKα radiation (λ = 1.54056 Å) operating at 40 kV and 40 mA. XRD patterns were collected in 2θ = 10°–65°. Raman spectra of powder samples were obtained with a Renishaw in via Raman microscope and excitation was achieved by using an argon ion laser (514 nm). X-ray photoelectronspectroscopy (XPS) was performed to analyze the surface elemental compositions of materials by using Thermo Scientific K-Alpha (See SM for details).

2.4. Electrode preparation and electrochemical measurements

All the electrochemical measurements were performed at room temperature using rotating disk electrode (RDE) equipment purchased from Pine Instruments connected to an Autolab (Ecochemie Inc. model-PGSTAT 30) bipotentiostat with a typical three-electrode electrochemical set up. For electrochemical measurements, the solutions were saturated with either high purity O_2 or Ar. During the experiments the gas flow was maintained over the solution. An Ag/AgCl (0.1 M KCl, 0.28 V vs. RHE) served as a reference electrode and all the potentials are referred to this electrode, and converted to RHE using the Nerst equation. Pt gauze was used as a counter electrode. The catalyst coated glassy carbon (GC) disk (5.6 mm diameter, 0.246 cm^2) was fabricated by casting catalyst ink and served as working electrode. Catalyst inks were prepared by ultrasonically dispersing the catalyst powder (3.1 mg) in a 0.936 mL solution of nafion (5 wt%, DuPont): DI water: isopropanol by volume ratio of 1:25:75. Typically, 15 μL (3.3 mgmL^{-1}) well dispersed catalyst ink were coated on the GC disk surface using a microsy-

Table 1
Concentrations of different nitrogen species on the surface of N-GN catalysts.

Sample	Pyridinic N% (atom%)	Pyrrolic N% (atom%)	Graphitic N% (atom%)	Pyridine-N oxide (atom%)
N-GN15	39	26	22	13
N-GN10	37	25	16	22
N-GN5	45	25	12	18

Table 2
Surface atomic concentrations of GO, rGO and N-GN catalysts.

Sample	Carbon% (atom%)	Oxygen% (atom%)	Nitrogen% (atom%)
GO	78.0	16.9	–
rGO	93.8	1.74	–
N-GN15	87.6	5.52	2.48
N-GN10	88.3	6.34	1.75
N-GN5	88.9	5.93	0.96

ringe and allowed to dry at room temperature. Catalyst loadings were kept constant to avoid any variations related to catalyst loading onto GC. Loadings employed were 102 $\mu g\,cm^{-2}$ N-GN catalysts or 25 $\mu g\,cm^{-2}$ Pt/C catalyst of geometric area on a GC disk.

3. Results and discussions

3.1. Physicochemical characterization

In the synthesis procedure of N-GN catalysts (Fig. 1), at first GO/melamine mixture was sonicated to exfoliate the GO sheets and to adsorb the melamine molecules onto GO sheets through π–π dispersion forces and hydrogen bonding between melamine and graphitic structure of GO [25]. After adjusting the pH value to 12, the temperature was increased to 85 °C for gelation of the mixture. At this temperature, Co^{+2} was added to catalyst the gelation. This process can facilitate possible covalent bonding between amino groups of melamine and carbonyl groups on GO sheets and also prevent the reagregation of GO sheets. After adjusting the pH value to 2, bright-black solid was obtained. Finally, grinded, washed and dried mixture was annealed under Ar atmosphere at 1050 °C for 1 h. Thermogravimetric analysis results of GO and GO-melamine mixtures containing different amounts of GO, which were performed in Ar flow, are shown in Fig. S2. It is seen that GO is stable almost below 700 °C. Slight weight loss was observed above 700 °C, which could be due to the decomposition of oxygen functional groups exists on GO sheets. Weight losses observed below 200 °C arise from the evaporation of the adsorbed water. All GO/melamine mixtures displayed almost similar thermogravimetric behaviors. Major weight looses for mixtures observed between 200 and 600 °C are assigned to the decomposition of melamine to NH_3 and alkylamine derivates. It must be noted that, the yield of the process depends on the initial GO ratio and increases with the initial percentage of GO in the mixture (Fig. S1). For example, ~1.5 g N-GN catalyst was obtained from the pyrolysis of 10 g 15% GO and 85% melamine mixture (N-GN15). We believe that this process could be scaled up for larger synthetic yields.

The surface morphology of control sample (rGO) and N- GN15 catalyst analyzed by SEM. The SEM images of the N-GN15 and rGO are shown in Fig. 2. The rGO contains flakes and three-dimensional (3D) particles that have size of tens of nanometers assembled by several pieces of graphene sheets. After the nitrogen doping process, typical crumpled silk veil wave-like morphology and mesoporous architecture of graphene structure was observed. This reveals a high exfoliation degree and prevents the restacking of sheets in evidence (Fig. 2b). The porous features of the GO, rGO and N-GN15 were investigated by isothermal N_2 adsorption/desorption measurements (Fig. 3a). The type-IV behavior shows the mesoporous structure was observed in the N_2 adsorption/desorption isotherm curves. The steep increase in nitrogen adsorption for N-GN15 and rGO at a relatively high pressure ($P/P^\circ = 0.85–0.99$) clearly suggests that the pore volume is mainly contributed by size-enlarged mesopores [26]. Such porous structure arose from the wrinkles and folds of the graphene nanosheet, and the prevented stacking between the neighboring graphene sheets, which was confirmed by the well-dispersed state of the N-GN15 in SEM (Fig. 2b). BET specific surface area (S_{BET}) of N-GN15 catalyst was measured as 585 $m^2\,g^{-1}$, which was much higher than those of the rGO (491 $m^2\,g^{-1}$) and GO (186 $m^2\,g^{-1}$). The gaseous thermal decomposition products of melamine, adsorbed between graphene plates, promote the exfoliation of graphene plates resulting an increase in S_{BET} values from rGO to N-GN15. It is to be noted that, pore structure containing macropores and mesopores in the carbon framework is very important from the perspective of fuel cells because it can facilitate the diffusion and transport of reactants, and provide more active sites for the ORR.

Structural information regarding the catalysts was obtained by using XRD. Fig. 3b shows the XRD patterns of the GO, rGO and N-GN15 catalysts. The characteristic (0020) diffraction peak located at approximately 26.5 for all samples [powder diffraction file (PDF) number 97-002-9123] indicates a layer-to-layer d-spacing of 0.34 nm and was attributed to diffraction of graphitic structure. The calculated full width at half maximum (fwhm) values at $2\theta = 26.5$ were 0.83, 0.94 and 1.21 for GO, rGO and N-GN15, respectively. The increasing trend of fwhm as GO < rGO < N-GN15 indicates the broadening of the peak and suggest the expanded graphene layers [19]. Significantly, the broad peak at 43.7, which corresponds to (101) diffraction of low graphitic degree, was disappeared in the N-GN15. This implies the N doping of GO and rearrangement of the graphitic structure through this process [19]. Raman spectroscopy is the direct and nondestructive technique to characterize the structure and the quality of carbon materials particularly to determine the defects, the ordered and disordered structures, and the layers of graphene. Raman spectra of samples were collected at an excitation wavelength of 514 nm under ambient conditions from the powders on Si substrates. For comparison, the spectra of GO and rGO were also collected. The Raman spectra of N-GN15 exhibits two remarkable peaks at around 1345 and 1575 cm^{-1} (Fig. 3c) corresponding to the well-defined D band and G band, respectively. As it is known, the G band related to the E_{2g} vibration mode of sp^2 carbon domains can be used to explain the degree of graphitization, while the D band is associated with sp^3 and sp carbon networks where is mostly at edges of the hexagonal lattice of graphene. In addition, D′ appears as a shoulder around 1610 cm^{-1} on the G band of GO, which is also a characteristic of weak disorder on the graphitic structure [27]. It is reported that the more disordered phase in the pristine carbon, the easier for N-doping effect, because the disordered phase is more reactive than the graphitic phase during the heat treatment and help fix nitrogen atoms in the carbon structure [28]. Hence, GO is favorable for N-doping. Also, D′ has disappeared with N doping (Fig. 3c.) suggesting the restored graphene structure. The intensity ratio (I_D/I_G) of the D to G bands is widely used for characterizing the defect quantity and N doping level in graphitic materials. The I_D/I_G value of GO (0.70) decreases to 0.47 for rGO and 0.58 for N-GN15. This indicates that partial sp^2 domains were restored at different levels, and the graphitic degree of NG samples was also improved accordingly due to the reduction effect and

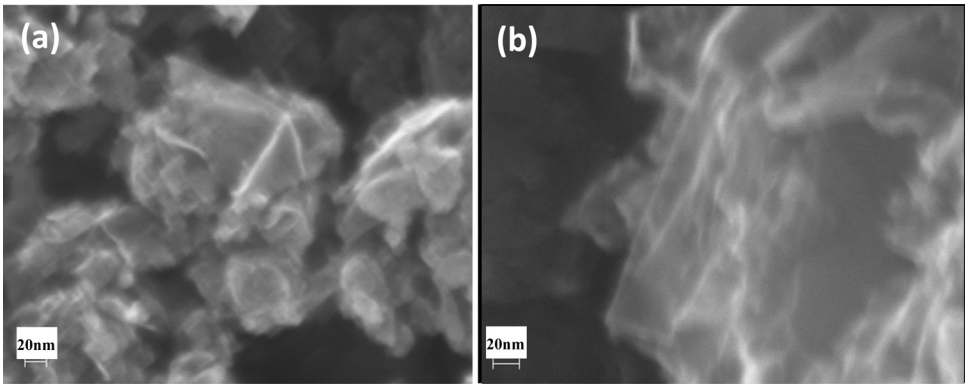

Fig. 2. SEM images of rGO (blank sample) (a) and N-GN15 catalyst (b).

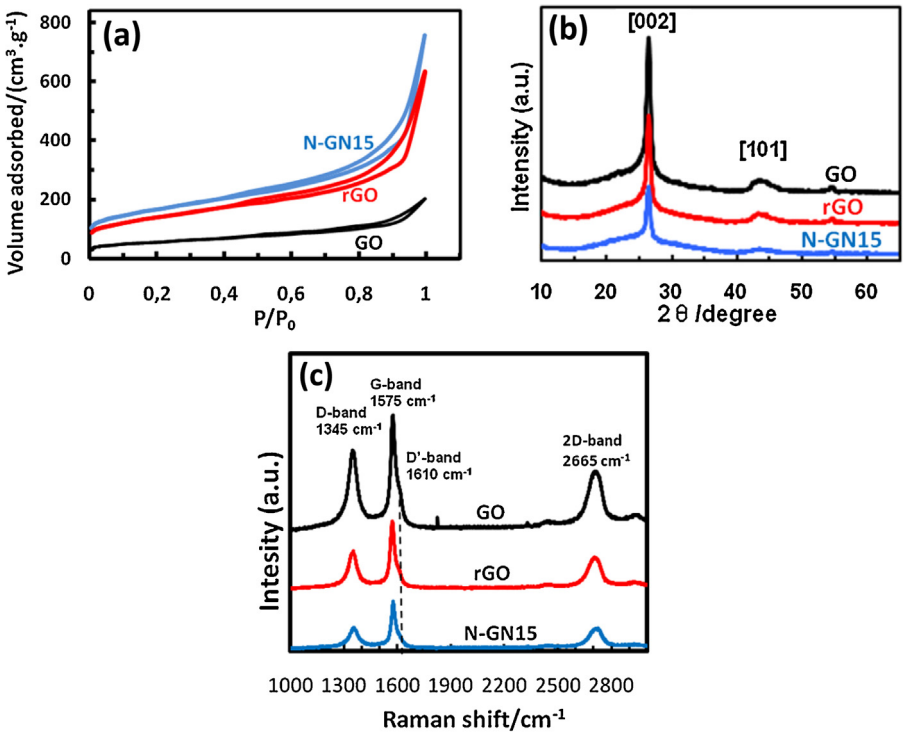

Fig. 3. Nitrogen adsorption/desorption isotherms (a), XRD patterns (b) and Raman spectra (c) of GO, rGO and N-GN15 catalyst.

"self-repairing" of the graphene layer at high temperature, which is also consistent with the XRD and SEM results. The 2D peak is the most prominent feature of graphene in the Raman spectrum, and its position and shape can be used to clearly distinguish between single-layer, bi-layer, and few-layer graphene [29]. For the N-GN15, the 2D peak appears at around 2665 cm^{-1} and the intensity of 2D was decreased with respect to the GO. Comparing with the spectrum of single-layer graphene [30], the present N-GN15 exhibits a broader and up-shifted peak in the Raman spectra, demonstrating that the N doping process results in few-layer N doped graphene nanosheets as observed in SEM images.

XPS characterizations were further performed to analyze the surface elemental composition and nitrogen bonding configurations of samples. The wide scan spectra of GO, rGO, N-GN15 are shown in Fig. 4a and collectively with N-GN10 and N-GN5 in Fig. S3. As can be seen, the wide scan XPS spectra of GO and rGO show only the presence of carbon and oxygen atoms. The high resolution C1s peak was centered at 285.1 eV, O1s at 533.3 eV and N1s at 399.7 eV for all samples. The asymmetric nature of high-resolution C1s spectra of N-GN15 (Fig. 4b) visually shows the incorporation of N atoms onto graphene surface and indicates the different carbon configurations by fitting with binding energies centered at: C=C (284.7 eV), C—O/C=N (286.6 eV), C=O/C—N (288.0 eV) and C—C (287.5 eV). The high-resolution N1s XPS spectrum for N-GN15 is shown in Fig. 4c. Similarly, the high-resolution N1s XPS spectra for N-GNs can also be well-fitted into four peaks: pyridinic N (398.6 eV), pyrrolic N (400.3 eV), graphitic N (401.4 eV) and pyridine-N oxide (403.3 eV). As shown in Fig. 4d, the graphitic nitrogen corresponds to N atoms that are linked with three carbon atoms in graphene basal plane, replacing the C atoms in graphene hexagonal ring [31]. Pyrrolic N occurs in five-member ring and can contribute to the π-conjugated system in the graphene layers with two π-electrons [19]. Pyridinic N occurs in six-member ring and can donate one π-electron to the aromatic π system [19]. Contents of surface nitrogen binding configurations of N-GNs, calculated by peak fitting based on Shirly base line, are collectively given in Table 1 and surface atomic concentrations of samples are given in Table 2.

The calculated surface total N content of N-GN15 was 2.48 atom%, from which pyridinic N is the main component and constitutes 39 atom%, graphitic N 22 atom%, pyrrolic N 26 atom% and

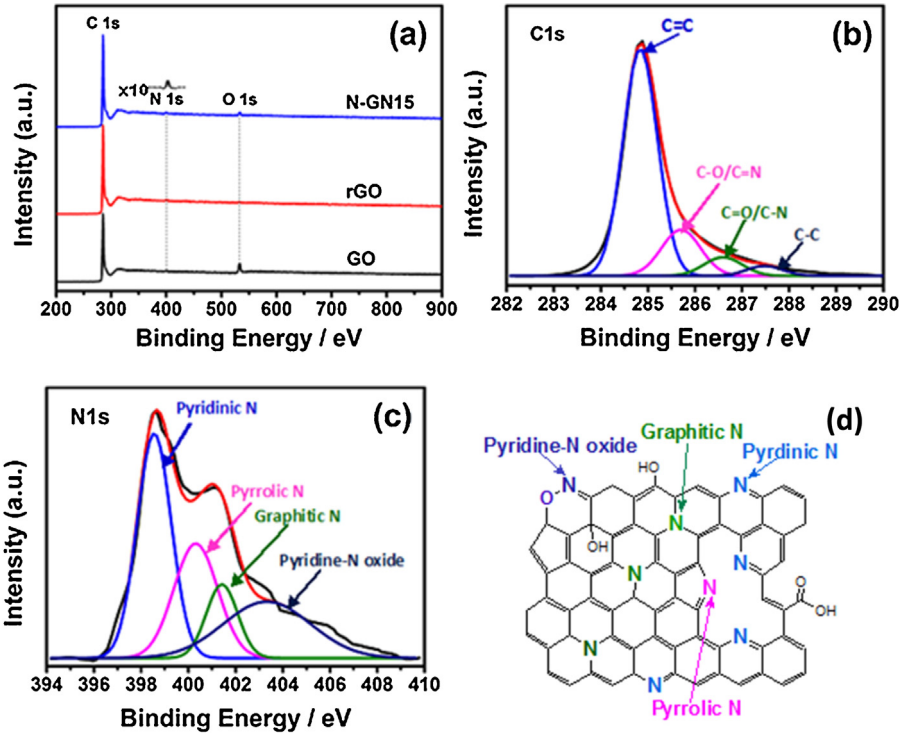

Fig. 4. XPS survey spectra for N-GN15 catalyst, rGO and GO (a). Inset is the tenfold N1s intensity of N-GN15 catalyst for visibility. High resolution C1s (b) and N1s (c) spectra of N-GN15 catalyst. Schematic structure of N-GN (d).

pyridine-N-oxide 13 atom%. Although pyridinic N is the main component in all N-GN catalysts, no correlation was observed between the GO content of initial mixture and the amount of the type of N groups exist in N-GNs except graphitic N, which decreases with the GO content of initial mixture. From Table 2, that surface oxygen concentration of GO substantially decreased from 16.9 atom% to 1.74 atom% in rGO due to the removal of oxygen functional groups during thermal treatment. However, surface oxygen concentrations of N-GNs are higher than that of the rGO when the samples are prepared at the same conditions. This is probably the result of the coverage of graphene plates with melamine gel, which prevents the removal of oxygen functional groups and formation of the N-O groups during pyrolysis of mixture. The higher percentage of melamine (e.i. lower GO content) led to formation of more carbon residues on graphene plates [25] clarifying the decrease in nitrogen content of N-GNs with decrease of GO percentage of initial mixture (Table 2). This can present a route for tailoring the surface nitrogen concentration of GO. Combining the XPS results with the above S_{BET}, Raman and XRD analysis, nitrogen doped graphene with increased SSA can be successfully synthesized by the proposed process. It is important to be noted that any metal impurities was not detected in XPS survey and XRD pattern of N-GNs.

3.2. Cyclic voltammetry studies

Electrochemically accessible surface area has crucial importance of a given catalyst since graphene sheets tend to stack together through π–π interaction during the application [21,22] which blocks a substantial amount of catalytic sites on graphene and inevitably decreases the catalytic activity. To confirm the increase in electrochemically accessible surface area of N-GN15 over rGO, cyclic voltammetry (CV) studies were performed in 0.1 M KOH and 0.1 M $KClO_4$ solutions at a scan rate of 15 $mV.s^{-1}$. Solutions are saturated with Ar to exclude the contribution of pseudocapacitance originated from the ORR. CVs, recorded after five activation cycles, are shown in Fig. 5a,b. Rectangular shape of CVs especially in acidic media reflects the ideal capacitative behavior of the samples. Reversible hump appeared in CV of N-GN15 in acidic media at around 0.6 V is originated from the oxidation/reduction of surface functional groups [32], which is consistent with the XPS results. The increased voltammetric responses over rGO to N-GN15 in both acidic and alkaline media are attributable to the contribution of the surface functional groups and increased SSA upon preventing the reaggregation of graphene sheets by the applied procedure, as reflected to the S_{BET} values of rGO and N-GN15. Specific capacitances of rGO and N-GN15 were calculated as previously [32] to quantify the voltammetric responses. These values are 116 $F\,g^{-1}$ for N-GN15 and 95 $F\,g^{-1}$ for rGO in acidic and 105 $F\,g^{-1}$ for N-GN15 and 44 $F\,g^{-1}$ for rGO in alkaline media. The decrease in specific capacitance value for both rGO and N-GN15 from acidic to alkaline media is ascribed to the weak interactions between OH^- ions and electron rich graphene layers, higher electronic charge density in the acidic electrolyte, and favorability of proton adsorption in the acidic electrolyte by the nitrogen functional groups [33].

3.3. Electrocatalytic activity and kinetics of N-GNs towards ORR

The electrocatalytic behavior of N-GN15 towards ORR was first assessed using CV at a potential scan rate of 15 $mV\,s^{-1}$ in 0.1 M $HClO_4$ and 0.1 M KOH solutions saturated with either Ar– or O_2–. Featureless voltammetric currents are observed in Ar-saturated solutions at the potential range of studied, whereas the reduction of oxygen occurs with appearing a sharp peak at 0.72 V in acidic and at 0.86 V in alkaline solutions when electrolyte is being saturated with O_2 (Fig. 5a,b), implying the electrocatalytic activity of N-GN15 towards ORR. The reduction peak at 0.72 V in acidic electrolyte is more positive than those of the metal containing [34] and metal free [35] nitrogen doped graphene, and 0.86 V in alkaline solution is much positive than those of the various nitrogen doped graphene-based [18,21,35] electrocatalysts, highlighting low overpotential

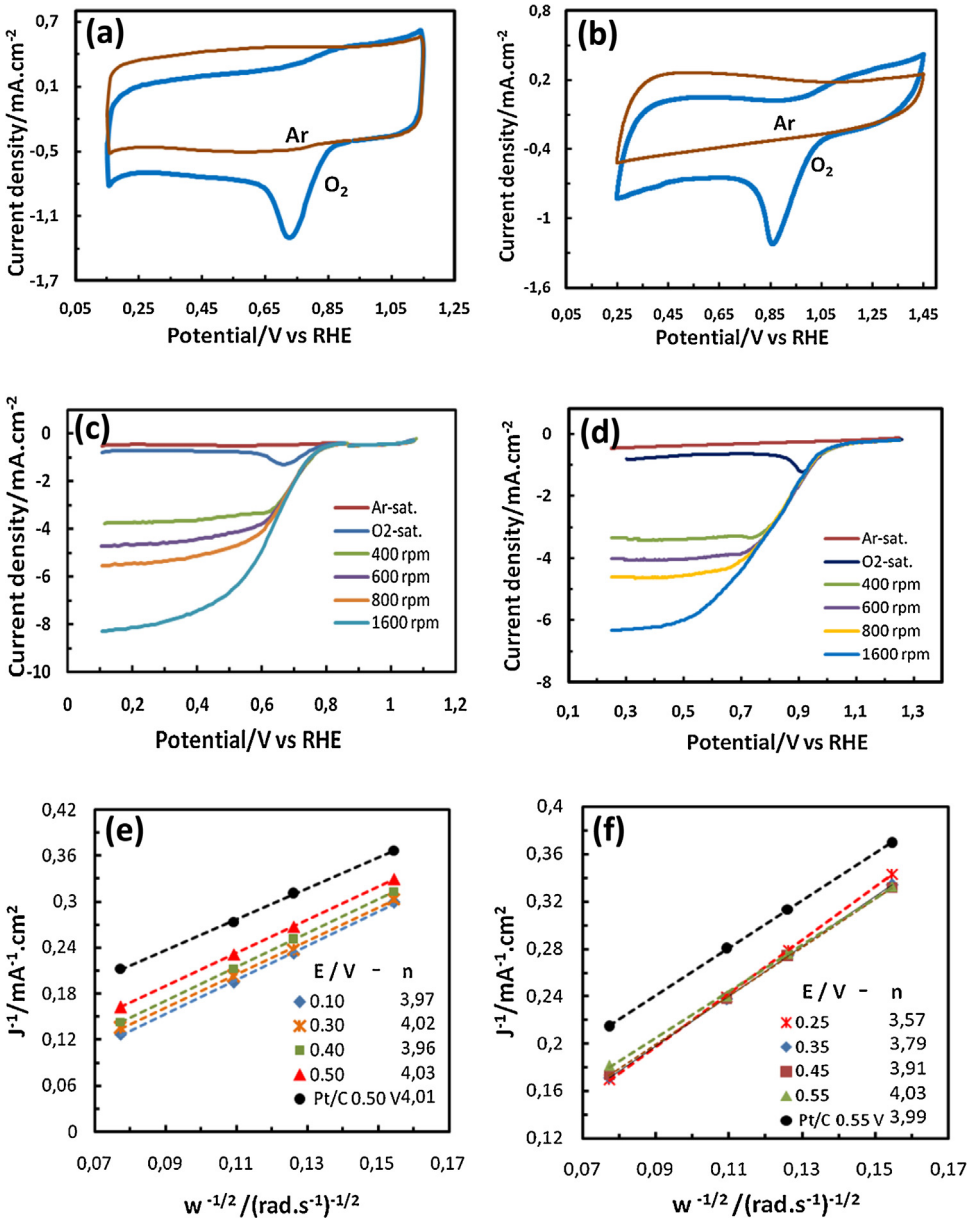

Fig. 5. Cyclic voltammograms of N-GN15 catalyst recorded in 0.1 M $HClO_4$ (a) and 0.1 M KOH (b) electrolytes at a scan rate of 15 mV s^{-1}. Rotating disk electrode (RDE) voltammograms of N-GN15 catalyst in O_2-saturated 0.1 M $HClO_4$ (c) and 0.1 M KOH (d) electrolytes at a scan rate of 15 mV s^{-1} with different rotation rates from 0 to 1600 rpm. Ar backgrounds are shown for clarification. Koutecky-Levich (K-L) plots of N-GN15 obtained with the data in O_2-saturated 0.1 M $HClO_4$ (e) and 0.1 M KOH (f) electrolytes. Insets of (e) and (f) indicate the number of electron transferred per mole of oxygen at the specified potentials.

for ORR applications. Further studies with N-GN15, N-GN10 and N-GN5 catalysts were carried out to gain further insight into the reaction kinetics and number of the electron transferred for per oxygen molecule on N-GNs using RDE voltammetry at different rotation rates (from 400 to 1600 rpm), and linear sweep voltammetry (LSV) curves were recorded at a potential scan rate of 15 mV s^{-1}. The results obtained for N-GN15 in O_2-saturated 0.1 M $HClO_4$ and 0.1 M KOH solutions are shown in Fig. 5c and Fig. 5d, respectively. The results for N-GN10 and N-GN5 are demonstrated in Fig. S5a-d. Background data obtained in Ar-saturated solutions are also shown in these figures. It is obvious that the N-GNs showed well-defined plateaux of diffusion limiting current densities below ~0.55 V in both acid and alkaline electrolytes at all rotational speeds, indicating an efficient surface electrocatalytic reaction with a direct four-electron transfer pathway [36]. Also, the diffusion limiting current densities significantly rise following the increase of rotation rates, as high rotation rates lead to a faster oxygen flux to electrode surface and consequently large currents, owing to the shorted diffusion length.

To investigate the ORR performances of N-GNs more quantitatively, the kinetic analysis was carried out by the Koutecky-Levich (K-L) equation [34] (see SM for details). The K-L plots (j^{-1} vs.$\omega^{-1/2}$) obtained from the LSV diffusion limiting current densities in 0.1 M $HClO_4$ and 0.1 M KOH electrolytes are shown in Fig. 5c and Fig. 5d, respectively. The results for N-GN10 and N-GN5 are also shown in Fig. S6a-d. The number of electrons transferred (n) calculated from the slope of K-L plots at the typical potentials is also marked in these figures. Note that, all current densities are corrected by subtracting the Ar data. Correlation coefficients for all K-L plots were greater than 0.99. To emphases the importance of doping effects on ORR activity in the region of real fuel cell application, we chose the potential of 0.50 V for 0.1 M $HClO_4$ and 0.55 V for 0.1 M KOH to com-

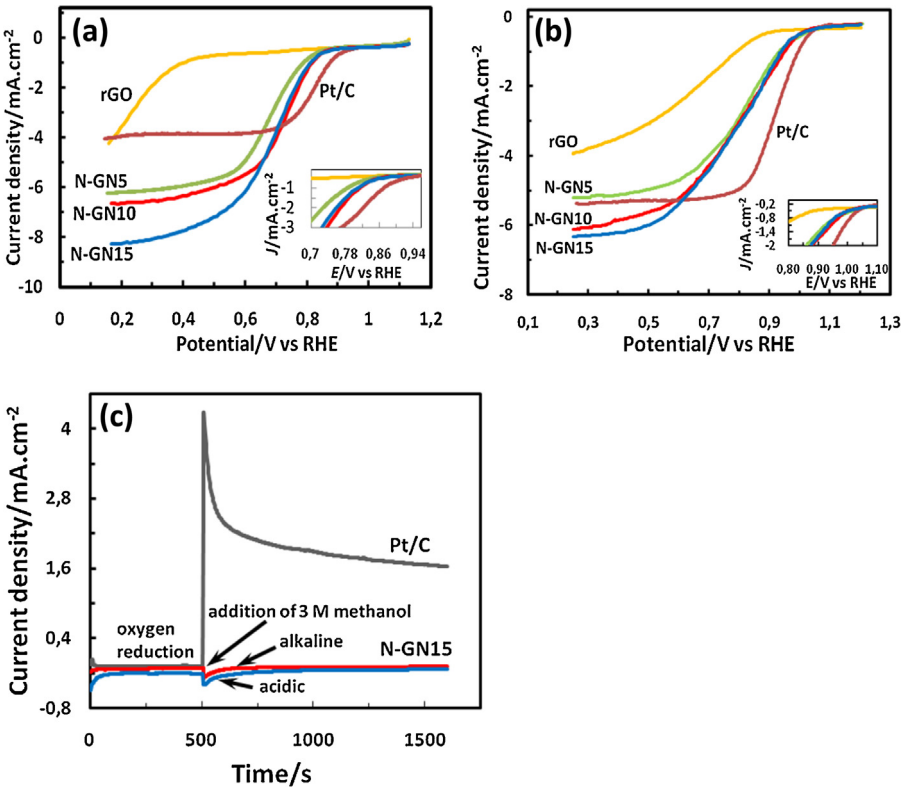

Fig. 6. Rotating disk electrode (RDE) voltammograms of rGO, N-GN5, N-GN10, N-GN15 and commercial Pt/C catalysts in O_2-saturated 0.1 M $HClO_4$ (a) and 0.1 M KOH (b) electrolytes at a scan rate of 15 mV s^{-1} and a rotation rate of 1600 rpm. Inset is the zoom-in of the voltammetric profiles. Chronoamperometric responses of N-GN15 and Pt/C in O_2-saturated alkaline electrolyte at −0.50 V and of N-GN15 in O_2-saturated acidic electrolyte at −0.55 V for ORR (c).

pare the electron transfer numbers with that of the commercial Pt/C (Tanaka, 46%), which are very high potential compared to the general viewpoint [37]. It can be seen that the all N-GN catalysts show electron transfer number close to the highly desired four-electron ORR pathway of maximum energy capacity within a wide potential range, indicating almost reduction of oxygen to H_2O in acidic and to OH^- in alkaline media [18] similar to the Pt/C catalyst. To support the results from RDE data and K-L plots, rotating ring-disk electrode (RRDE) studies were performed to detect the hydrogen peroxide generation during ORR process (see SM for details). RRDE polarization curves, obtained from the N-GN15 catalyst, are shown in Fig. S7. The electron transfer numbers (n) calculated from RRDE data at specified potentials are tabulated in Table S1 together with those calculated from K-L plots for comparison. The closeness of n values to those calculated from K-L plots further confirms the four-electron process in both acidic and alkaline electrolytes. Although the total nitrogen content of prepared catalysts decreases in the order of N-GN15 > N-GN10 > N-GN5 (Table 2), it is found that the total nitrogen content of our N-GNs did not affect the electron transfer number for ORR in both acidic and alkaline electrolytes. Notably, the electron transfer number for rGO (Data not given) changed in the range of 1.7–2.1 electrons per mole of oxygen in both acidic and alkaline electrolytes, which is consistent with the literature [18,19,27]. K-L plots of N-GN15 (Fig. 5e,f), N-GN10 (Figs.S6a,b) and N-GN5 (Figs.S6c,d) at different potentials show fine linearity and parallelism, indicating the first-order reaction kinetics for ORR with respect to the concentration of dissolved oxygen [38] and consistent with the electron transfer numbers at different potentials. Fine parallelism of K-L plots of all N-GNs to commercial Pt/C also confirms the four-electron pathway for ORR at specified potentials.

3.4. Evaluation of electrocatalytic activity of N-GNs towards ORR

LSV curves of samples are plotted at a fixed rotation rate of 1600 rpm and a potential sweep rate of 15 mV s^{-1} to evaluate the ORR performances and investigate the role of nitrogen doping configurations on ORR performances of N-GNs in terms of onset potential and diffusion limiting current densities which have great importance in real applications of ORR in fuel cells and other electrochemical devices. The LSV curves of all samples are shown in Fig. 6a and Fig. 6b for O_2-saturated acidic and alkaline electrolytes, respectively. The blank sample (rGO) exhibits oxygen reduction with an onset potential of ~0.42 V in acid electrolyte and 0.87 V in alkaline electrolyte similar to that of the edge functionalized few layer graphene [39]. It is also more positive than that of various nitrogen-doped graphene [40,41], highlighting nanosized graphene with a highly crystalline basal plane, and edge functionalized groups with only a low amount of oxygen content, which is consistent with the physicochemical characterization results. The onset of rGO in alkaline electrolyte is very positive than the one in acidic medium. This can be ascribed to the increase of the electronic charge density of a highly crystalline basal plane through thermal reduction of GO which favors the adsorption of H^+ rather than oxygen in acidic electrolytes [42] resulting in a lower onset for ORR with respect to the alkaline electrolyte. Expectedly, incorporation of nitrogen atoms into graphene structure results in a shift on the onset potential to more positive potentials in acidic electrolyte exhibiting an onset potential of 0.84 V, 0.86 V and 0.87 V for N-GN5, N-GN10 and N-GN15, respectively (inset of Fig. 5a). The shift in onset potentials from rGO to N-GNs upon nitrogen doping in alkaline electrolyte was relatively small (~135 mV) and all N-GN catalysts showed almost equal onset potentials of 1.01 V in alkaline electrolyte (Fig. 5b). The onset potential of N-GN15 is only 70 mV negative than that of high quality (46% Pt content)

Pt/C (0.87 V vs. 0.94 V) in acidic and 40 mV (1.01 V vs. 1.05 V) in alkaline electrolyte showing a comparable electrochemical ORR activity on the basis of onset potential. The huge enhancement of onset especially in acidic electrolyte supports the previous findings based on quantum mechanics calculations indicating the high eletronegativity of nitrogen in the graphene framework, which can induce positive charge density on an adjacent C atom and facilitate oxygen adsorption, subsequently weaken the bonding in the oxygen molecule [43]. There is no doubt that the incorporation of nitrogen into graphene structure increases the ORR performance of graphene. However, there is still a controversy on the role of nitrogen types on ORR. The investigation of oxygen molecule dissociation energy barrier has shown that it can be reduced by all types of nitrogen and the graphitic N reduces the energy barrier more efficiently than the pyridinic N, which might be one of the reasons for improved electrocatalytic activity of N-doped carbon catalysts [44]. It is stated that the content of graphitic N greatly increases the limiting current density and pyridinic N is responsible for improving the onset potential and converting the ORR mechanism from 2-electron pathway to 4-electron process [45,46]. On the basis of our results pyridinic N is the main component in all N-GN catalysts and graphitic N content decreases in the order of N-GN15 > N-GN10 > N-GN5 (Table 1) which is the same order of diffusion limiting current densities, those are 7.98 mA.cm^{-2} > 6.19 mA cm^{-2} > 5.74 mA cm^{-2} for acidic electrolyte and 5.93 mA cm^{-2} > 5.67 mA cm^{-2} > 4.78 mA cm^{-2} for alkaline electrolyte. It is obvious that the graphitic N content is responsible from the current densities of nitrogen doped graphene catalysts for ORR, which is consistent with the literature [44,45]. Interestingly, the diffusion limiting-current densities of all N-GNs are higher than that the Pt/C (4.06 mA cm^{-2} in acidic electrolyte and 5.36 mA cm^{-2} in alkaline electrolyte) except the one for N-GN5 in alkaline electrolyte (Fig. 6a,b) and it is almost two orders of magnitude higher than that of Pt/C for N-GN15 in acidic electrolyte. Besides the N-doping effect, the increased magnitude in diffusion limiting-current densities and close onset potentials to Pt/C of N-GN catalysts are most likely the result of increased electrochemically accessible surface area by preventing reaggregation and edge functionalization of GO sheets which stabilizes ORR intermediates such as H_2O_2 in porous structure and promotes the direct four-electron pathway for ORR [47,48].

On the other hand, it is important to take into account the Co content of resultant N-GNs, since trace amounts of metal species can improve performance of the catalyst. Any metal impurities were not detected in XPS survey and XRD pattern of our N-GNs (Section 3.1). Inductively coupled plasma mass spectrometry (ICP-MS) measurements were further performed to determine the Co content of N-GN15 (see SM for details). For N-GN15, only 0.068 ± 0.021% (w/w) Co was detected. Recently, Sha et al. found that the electrocatalytic ORR performances of nitrogen doped carbons increase with Co content and 1,0% (w/w) of Co content was found as an optimum value for Co-N_x-C type ORR catalysts [34]. Thus, Co-N active sites, could have contributed to the electrocatalytic performance of N-GN15 to a limited extent.

3.5. Methanol tolerance of N-GN15 catalyst

In fuel cells, the selectivity of catalyst towards ORR is of great significance since fuel molecules such as methanol in the anode may permeate through the polymer membrane to the cathode, which could seriously affect the performance of the cathode catalysts. Thus, the N-GN15 catalyst is further subjected to testing the methanol tolerance ability in O_2-saturated 0.1 M KOH and $HClO_4$ electrolytes at potentials of 0.50 V and 0.55 V, respectively, toward ORR via a current–time (i–t) chronoamperometric method. As shown in Fig. 6c, the original cathodic current of N-GN15 remained almost unchanged even after the addition of 3 M methanol into the electrolyte solutions. In contrast, the corresponding anodic current on commercial Pt/C electrode in alkaline electrolyte increases sharply upon addition of methanol. This result unambiguously suggests that the N-GN15 electrocatalyst exhibits good selectivity for ORR thus being superior to the commercial Pt/C electrocatalyst in both acidic and alkaline electrolytes.

4. Conclusions

Nitrogen doped graphene based electrocatalyst have been successfully synthesized through a solution-based two-step scalable procedure by thermal treatment of GO/melamine gel composite. The SSA thus electrochemically accessible surface area of N-GN15 catalyst has been appreciably increased by using melamine as spacer. The N-GN15 catalyst exhibited comparable onset potential, larger diffusion-limiting current density and excellent methanol tolerance capability over the commercial Pt/C catalyst towards ORR in both acidic and alkaline electrolytes. It is found that the graphitic N content is responsible for the increasing limiting current density of N-GN catalysts.

Acknowledgement

The support of this work by the Scientific Research Projects Coordination Unit of Akdeniz University with project number of 2012.01.0115.009 is acknowledged. The XPS characterization was performed at the Center for Nanoscale Systems (CNS) at Harvard University. Dr. Cihan YILMAZ is also acknowledged for SEM measurements.

Appendix A. Supplementary data

Supplementary data associated with this article can be found, in the online version, at http://dx.doi.org/10.1016/j.apcatb.2016.03.043.

References

[1] V.R. Stamenkovic, B. Fowler, B.S. Mun, G.F. Wang, P.N. Ross, C.A. Lucas, N.M. Markovic, Science 315 (2007) 493–497.
[2] Z.Y. Lin, H.B. Chu, Y.H. Shen, L. Wei, H.C. Liu, Y. Li, Chem. Commun. 46 (2009) 7167–7169.
[3] S. Mukerjee, J. Appl. Electrochem. 20 (1990) 537–548.
[4] B. James, J. Kalinoski, K. Baum, http://www.hydrogen.energy.gov/pdfs/review10/fc018_james_2010_o_web.pdf.
[5] M. Winter, R.J. Brodd, Chem. Rev. 104 (2004) 4245–4269.
[6] M. Lefevre, E. Proietti, F. Jaouen, J.P. Dodelet, Science 324 (2009) 71–74.
[7] F.Y. Cheng, Y. Su, J. Liang, Z.L. Tao, J. Chen, Chem. Mater. 22 (2010) 898–905.
[8] K.P. Gong, F. Du, Z.H. Xia, M. Durstock, L.M. Dai, Science 323 (2009) 760–764.
[9] R.L. Liu, D.Q. Wu, X.L. Feng, K. Mullen, Angew. Chem. Int. Ed. 49 (2010) 2565–2569.
[10] Z. Lin, M. Song, Y. Ding, Y. Liu, M. Liu, C. Wong, Phys. Chem. Chem. Phys. 14 (2012) 3381–3387.
[11] K.S. Novoselov, A.K. Geim, S.V. Morozov, D. Jiang, Y. Zhang, S.V. Dubonos, I.V. Grigorieva, A.A. Firsov, Science 306 (2004) 666–669.
[12] A.K. Geim, K.S. Novoselov, Nat. Mater. 6 (2007) 183–191.
[13] S. Wakeland, R. Martinez, J.K. Grey, C.C. Luhrs, Carbon 48 (2010) 3463–3470.
[14] Q. Liu, H. Zhang, H. Zhong, S. Zhang, S. Chen, Electrochim. Acta 81 (2012) 313–320.
[15] L. Sun, L. Wang, C. Tian, T. Tan, Y. Xie, K. Shi, M. Li, H. Fu, RSC Adv. 2 (2012) 4498–4506.
[16] Z. Lei, L. Lu, X.S. Zhao, Energy Environ. Sci. 5 (2012) 6391–6399.
[17] L. Yang, S. Jiang, Y. Zhao, L. Zhu, S. Chen, X. Wang, Q. Wu, J. Ma, Y. Ma, Z. Hu, Angew. Chem. Int. 50 (2011) 7132–7135.
[18] Y. Zheng, Y. Jiao, M. Jaroniec, Y. Jin, S.Z. Qiao, Small 8 (2012) 3550–3566.
[19] Z.H. Sheng, L. Shao, J.J. Chen, W.J. Bao, F.B. Wang, X.H. Xia, ACS nano 6 (2011) 4350–4358.
[20] S. Shanmugam, T. Osaka, Chem. Commun. 15 (2011) 4463–4465.
[21] C. Zhu, S. Dong, Nanoscale 5 (2013) 1753–1767.
[22] J.C. Meyer, A.K. Geim, M.I. Katsnelson, K.S. Novoselov, T.J. Booth, S. Roth, Nature 446 (2007) 60–63.
[23] Y.Q. Sun, C. Li, G.Q. Shi, J. Mater. Chem. 12 (2012) 12810–12816.

[24] Y. Zhao, C. Hu, Y. Hu, H. Cheng, G. Shi, L. Qu, Angew. Chem. Int. Ed. 54 (2012) 11371–11375.
[25] Y. Sun, C. Li, Y. Xu, H. Bai, Z. Yao, G. Shi, Chem. Commun. 46 (2010) 4740–4742.
[26] X.D. Huang, K. Qian, J. Yang, J. Zhang, L. Li, C.Z. Yu, D.Y. Zhao, Adv. Mater 24 (2012) 4419–4423.
[27] I.Y. Jeon, H.J. Choi, S.M. Jung, J.M. Seo, M.J. Kim, L. Dai, J.B. Baek, J. Am. Chem. Soc. 135 (2012) 1386–1393.
[28] F. Jaouen, F. Charreteur, J.P. Dodelet, J. Electrochem. Soc. 153 (2006) A689–A698.
[29] X. Fu, J. Jin, Y. Liu, Z. Wei, F. Pan, J. Zhang, ACS Appl. Mater. Interfaces 6 (2014) 3930–3936.
[30] C.H. Lui, L. Liu, K.F. Mak, G.W. Flynn, T.F. Heinz, Nature 462 (2009) 339–341.
[31] H. Wang, T. Maiyalagan, X. Wang, ACS Catal. 2 (2012) 781–794.
[32] E. Bayram, E. Ayranci, Electrochim. Acta 56 (2011) 2184–2189.
[33] Y.H. Lee, K.H. Chang, C.C. Hu, J. Power Sour. 227 (2013) 300–308.
[34] H.D. Sha, X. Yuan, L. Li, Z. Ma, Z.F. Ma, L. Zhang, J. Zhang, J. Power Sour. 255 (2014) 76–84.
[35] M. Vikkisk, I. Kruusenberg, U. Joost, E. Shulga, I. Kink, K. Tammeveski, Appl. Catal. B: Environ. 147 (2014) 369–376.
[36] W. Wei, H. Liang, K. Parvez, X. Zhuang, X. Feng, K. Müllen, Angew. Chem. Int. Ed. 53 (2014) 1570–1574.
[37] Y. Zheng, Y. Jiao, L. Ge, M. Jaroniec, S.Z. Qiao, Angew. Chem. Int. Edit. 52 (2013) 3110–3116.
[38] G. Ma, R. Jia, J. Zhao, Z. Wang, C. Song, S. Jia, Z. Zhu, J. Phys. Chem. C 115 (2011) 25148–25154.
[39] B. John, X. Qian, W. Peng, S. Yuting, S. Litao, W. Tanyuan, L. Meixian, P. Pagona, ACS Appl. Mater. Interfaces 6 (2014) 19726–19736.
[40] T. Skaltsas, X. Ke, C. Bittencourt, N. Tagmatarchis, J. Phys. Chem. C 117 (2013) 23272–23278.
[41] Y. Zhang, J. Ge, L. Wang, D. Wang, F. Ding, X. Tao, W. Chen, Sci. Rep. 3 (2013) 2771–2778.
[42] E.J. Ra, M.H. Tran, S. Yang, T.H. Kim, C.S. Yang, Y.J. Chung, Y.K. Lee, I.J. Kim, H.K. Jeong, Curr. Appl. Phys. 14 (2014) 82–86.
[43] Z.Y. Lin, M.K. Song, Y. Ding, Y. Liu, M.L. Liu, C.P. Wong, Phys. Chem. Chem. Phys. 14 (2012) 3381–3387.
[44] S. Ni, Z.Y. Li, J.L. Yang, Nanoscale 4 (2012) 1184–1189.
[45] L.F. Lai, J.R. Potts, D. Zhan, L. Wang, C.K. Poh, C.H. Tang, H. Gong, Z.X. Shen, Y. Lin, R.S. Ruoff, Energy Environ. Sci. 5 (2012) 7936–7942.
[46] D. Guo, R. Shibuya, C. Akiba, S. Saji, T. Kondo, J. Nakamura, Science 351 (2016) 361–365.
[47] N. Ramaswamy, S. Mukerjee, Adv. Phys. Chem. 2012 (2012) 1–17.
[48] Y. Jiang, L. Yang, T. Sun, J. Zhao, Z. Lyu, O. Zhuo, X. Wang, Q. Wu, J. Ma, Z. Hu, ACS Catal. 5 (2015) 6707–6712.